Electronic Supplementary Material (ESI) for Journal of Materials Chemistry A.

Supporting Information

Metal-Organic Framework Derived Co_9S_8 Embedded in N, O and S-Tridoped Carbon Nanomaterials as Efficient Oxygen Bifunctional Electrocatalyst

Jin-Yan Zhao, Rui Wang, Shan Wang, Ya-Ru Lv, Hong Xu, Shuang-Quan Zang*

College of Chemistry and Molecular Engineering, Zhengzhou University, Zhengzhou 450001, China

*E-mail: zangsqzg@zzu.edu.cn

Experimental

Materials: Cobalt nitrate hexahydrate ($Co(NO_3)_2·6H_2O$, 99%), 1,4-Benzenedicarboxylic acid (H_2BDC, $C_8H_4O_4$, 99%), commercial Pt/C (Pt 20 wt.%) were obtained commercially and used without further purification. 4,4'-(sulfonylbis (4,1-phenylene)) dipyridine (SPDP, $C_{22}H_{16}N_2O_2S$, 99%) was synthetic by our own according the article.[S1] All the solvents used were of analytical grade.

Instrumentation and Measurements: PXRD patterns of the compounds were recorded on a Rigaku B/Max-RB X-ray diffractometer operating with Cu Ka radiation ($\lambda = 1.5418$ Å). Nitrogen sorption isotherms were measured at liquid nitrogen temperature (77 K) by using automatic volumetric adsorption equipment (Belsorp Max) after a degassed process at 100 °C for 12 h. Specific surface areas were obtained by using the Brunauer-Emmet-Teller (BET) model, pore size distributions were simulated by the nonlocal density functional theory (NLDFT) model, and the pore volumes were calculated from the amount adsorbed at P/P_0=0.99. Raman spectra were recorded on a LabRam HR Evolution with excitation from the 532 nm line of an Ar-ion laser. XPS measurements were performed using ESCALAB 250 system X-ray photoelectron spectrometer operating with a monochromatic Al Kα (300 W) X-ray resource. SEM images of the materials were obtained with Zeiss Sigma 500. The TEM, HR-TEM images and elemental distribution mapping images were obtained in FEI TalosF200S equipment.

Single-Crystal X-ray Diffraction Analysis (SCXRD): SCXRD measurements of **Co-MOF** was performed on a Rigaku XtaLAB Pro diffractometer with Cu-Ka radiation (λ=1.54178 Å) at 298 K. Data collection and reduction were performed using the program CrysAlisPro. The intensities were corrected for absorption using empirical method implemented in SCALE3 ABSPACK scaling algorithm. The structures were solved with intrinsic phasing methods (SHELXTS-2015) and refined by full-matrix least squares on F^2 using $OLEX_2$, which utilizes the SHELXL-2015 module. All non-hydrogen atoms were refined anisotropically, and the hydrogen atoms were included on idealized positions. The crystal structures were visualized by DIAMOND 3.2.

Synthetic of Co-MOF: 5 mg terephthalic acid, 11.2 mg SPDP and 13 mg $Co(NO_3)_2·6H_2O$ were dissolved in DMF (1 mL) and H_2O (0.5 mL). Then the solution was added to 6 mL glass vial which was heated at 90 °C for 48 h. Red crystals were obtained after cooling. Crystals were collected and dried at 90 °C overnight.

Synthetic of F-Co_9S_8 NPs: F-Co_9S_8 NPs used in this work was prepared in a typical procedure, 0.851g $CoSO_4·7H_2O$, 0.352g Na_2SO_3 were dissolved in the mixed solvents of 20 mL H_2O and 15 mL hydrazinium hydroxide, then the mixture was refluxed for 72 h at 180 °C to form the black precipitates. After collected by centrifugation and washed with water several times, the as-obtained precipitates were dried at 100 °C overnight.

Preparation of Co_9S_8@TDC: The ground Co-MOF powder was placed into a tube furnace and annealed at different temperatures (600, 700, 800, 900 °C) for 3 h with a heating rate of 10 °C min^{-1} under a flowing N_2. After tube furnace cooling to room temperature naturally, the calcined samples were collected and washed in 1 M hydrochloric acid for 24 h, the sample of powder obtained was washed by deionized water and ethanol several times respectively, then dried in a vacuum oven at 60 °C for 12 h.

Electrochemical measurements: The OER and ORR activities of the catalysts were comprehensively evaluated at room temperature using an electrochemical analyzer model CHI 660E and Wave driver + AFMSRCE, respectively. In this system, Ag/AgCl electrode as reference electrode, platinum electrode as counter electrode, GCE was used as the working electrode for loading catalysts ink. Before use, the working electrode was ground with a 0.05 μm polishing powder and ultrasonically rinsed with water, ethanol and dried naturally. The well-dispersed catalyst ink was prepared by dispersing 4.0 mg of catalyst in 120 μL of solution containing 100 μL of DMF and 20 μL of 5 wt.% Nafion solution followed by ultrasonication for 30 min. Applying the prepared catalyst slurry evenly on the working electrode. All potentials were calibrated by reversible hydrogen electrode (RHE) with reference to the RHE: E (RHE) = E (Ag/AgCl) + 0.198 + 0.059 × pH. All tests were not performed with current-resistance (*iR*) compensation.

OER performance tests: OER test were performed in 1 M KOH solution. Linear sweep voltammetry (LSV) measurements were recorded at a scan rate of 5 mV s^{-1} to obtain the polarization curves. The presented current density was normalized to the geometric surface area. 3 μL of the catalyst ink was pipetted onto the GCE surface (3mm in diameter, S = 0.0706 cm^2) by using a micropipettor and then dried at ambient temperature. The loading amount of catalyst was 1.4 mg cm^{-2} on the GCE. Electrochemical impedance spectroscopy (EIS) measurements were carried out from 50000 Hz to 0.01 Hz with an amplitude of 10 mV. The overpotential (η) was calculated according to the following formula:

$$\eta = \mathrm{E\,(RHE)} - 1.23$$

ORR performance tests: ORR tests were performed in 0.1 M KOH solution. Cyclic voltammetry (CV) measurements in N_2- or O_2- saturated electrolyte were performed at a sweep rate of 50 mV s^{-1}. Rotating disk electrode (RDE) measurements were performed by LSV at a sweep rate of 10 mV s^{-1} with various rotating speeds range from 400 to 2500 rpm. 10 μL of the catalyst ink was pipetted onto the RDE surface (5 mm in diameter, S = 0.1962 cm^2) by using a micropipettor and then dried at ambient temperature. The loading amount of catalyst is 1.7 mg cm^{-2} on GCE. The RDE and RRDE experiments were performed with MSR electrode rotator (Pine Instrument Co).

The K–L plots could be analyzed for determining the electron transfer number (n) at various electrode potentials.

$$\frac{1}{j} = \frac{1}{j_k} + \frac{1}{B\,\omega^{1/2}}$$

$$B = 0.2\,nF\,(D_{O_2})^{2/3}\,v^{-1/6}\,C_{O_2}$$

Where j_k is the kinetic current, j is the measured current density, ω is the angular velocity of rotating electrode ($\omega = 2\pi N$, N is the linear rotation speed), F is the Faraday constant (96485 C mol^{-1}), C_{O_2} is the bulk concentration of O_2 (1.2×10^{-6} mol cm^{-3}), Do_2 is the diffusion coefficient of O_2 (1.9×10^{-5} cm^2 s^{-1}), and v is the kinematic viscosity of the electrolyte (0.01 cm^2 s^{-1}) in 0.1 M KOH electrolyte.

$$n = \frac{4 \times j_d}{j_d + \frac{j_r}{N}}$$

$$H_2O_2\% = \frac{200 \times \frac{j_r}{N}}{j_d + \frac{j_r}{N}}$$

Where n is the electron transfer number, j_d is the disk current, j_r is the ring current and N is the current collection efficiency (0.37) of the Pt ring of RRDE electrode.

Zn-air battery performance tests: Zn-air battery assembly diagram was shown in Fig. 1. The Zinc plate was used as the negative electrode, and the foamed nickel uniformly (3 cm × 3 cm) supporting the catalyst was used as the positive electrode. About 3 mL electrolyte solution (6 M KOH/0.5 M $Zn(OAc)_2$) was added in the middle of the positive and negative electrodes. At the same time, the gas diffusion film was trapped outside the positive electrode in order to allow oxygen to enter the contact cathode material. The loading mass of catalyst on the foamed nickel is 3.5 mg cm^{-2}.

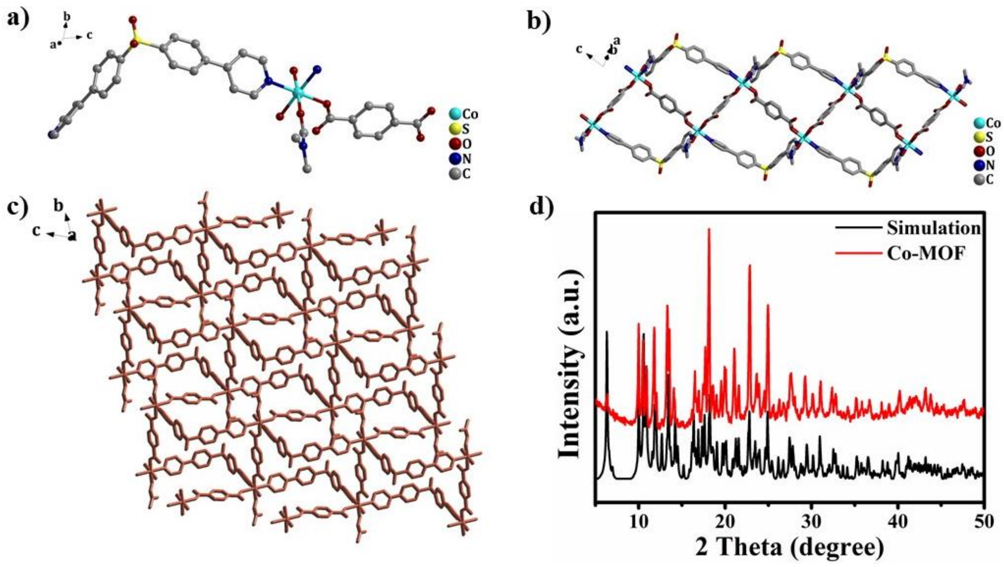

Fig. S1 a) The coordination environment of Co (II) in Co-MOF. b, c) 2D Single-layer of Co-MOF along with different axis; d) PXRD pattern of the as-synthesized Co-MOF.

Table S1 Crystallographic data and structure refinement for Co-MOF.

	Co-MOF
CCDC number	1867629
Empirical formula	$C_{33}H_{29}CoN_3O_8S$
Formula weight	686.58
Temperature / K	293 (2)
Crystal system	triclinic
Space group	P-1
A /Å	9.1585 (7)
B /Å	15.3205 (6)
C /Å	15.4803 (4)
α /°	64.375 (3)
β /°	83.258 (5)
γ /°	74.434 (5)
Volume /Å3	1886.61 (18)
Z	2
ρ calc g /cm3	1.209
μ /mm-1	4.483
F (000)	710.0
Crystal size /mm3	0.3 × 0.2 × 0.2
Radiation	Cu Kα (λ = 1.54184)
2Θ range for data collection /°	6.332 to 146.636
Index ranges	$-10 \leq h \leq 10$, $-19 \leq k \leq 16$, $-18 \leq l \leq 19$
Reflections collected	18569
Independent reflections	7288 [R int = 0.0549, R sigma = 0.0539]
Data /restraints /parameters	7288/0/418
Goodness-of-fit on F2	1.026
Final R indexes [I>=2σ (I)]	R1 = 0.0785, wR2 = 0.2236
Final R indexes [all data]	R1 = 0.0996, wR2 = 0.2425
Largest diff. peak/hole / e Å-3	1.25 / -0.52

Table S2 Elemental analysis for Co-MOF.

$C_{33}H_{29}CoN_3O_8S$ (%)	**C content**	**H content**	**N content**	**S content**
Theoretical	**57.72**	**4.26**	**6.12**	**4.67**
Measured	**56.34**	**4.70**	**6.45**	**4.03**

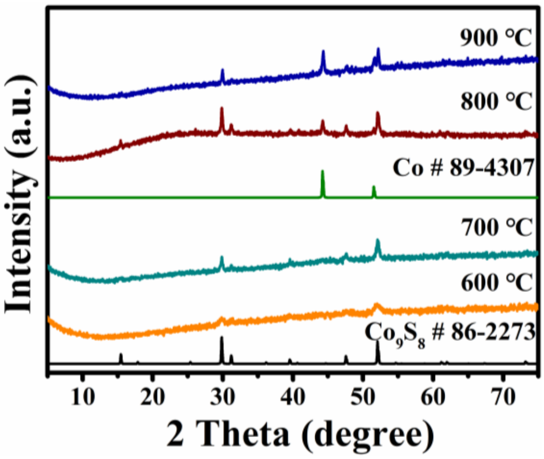

Fig. S2 PXRD patterns of hybrid materials calcined at different temperature (before hydrochloric acid etching).

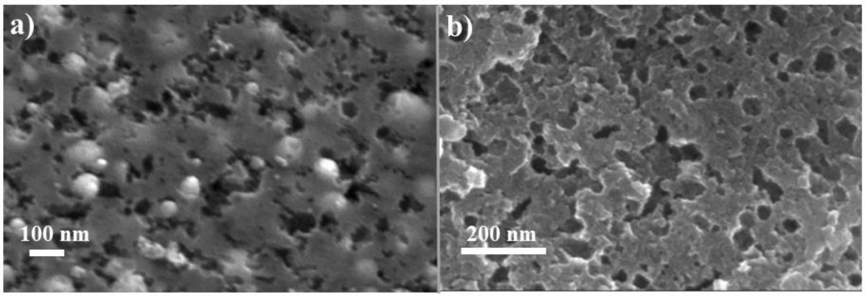

Fig. S3 a) SEM image of Co_9S_8@TDC-900 before washed; b) SEM image of Co_9S_8@TDC-900 after washed.

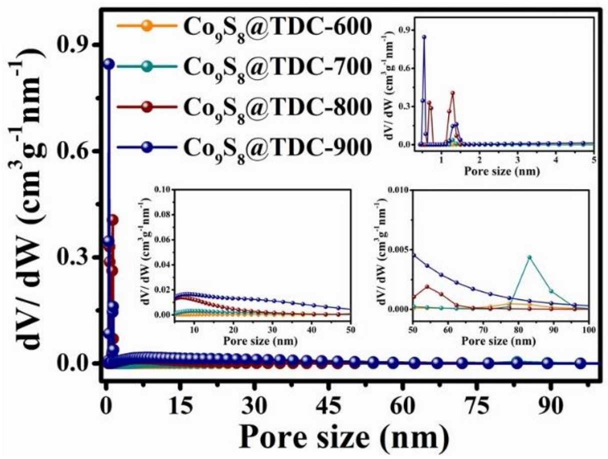

Fig. S4 Pore size distributions calculated by using NLDFT method.

Table S3 Specific surface area and total pore volume of the Co_9S_8@TDC materials.

Sample	$a_{s,\ BET}$ ($m^2\ g^{-1}$)	Total Pore Volume ($cm^3\ g^{-1}$)
Co_9S_8@TDC-600	16.86	0.03
Co_9S_8@TDC-700	22.66	0.10
Co_9S_8@TDC-800	31.45	0.32
Co_9S_8@TDC-900	247.2	0.62

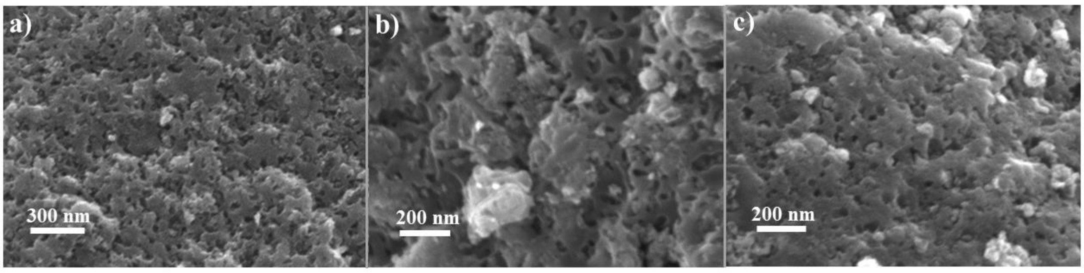

Fig. S5 SEM images of Co_9S_8TDC. a) Co_9S_8TDC-600; b) Co_9S_8TDC-700; c) Co_9S_8TDC-800.

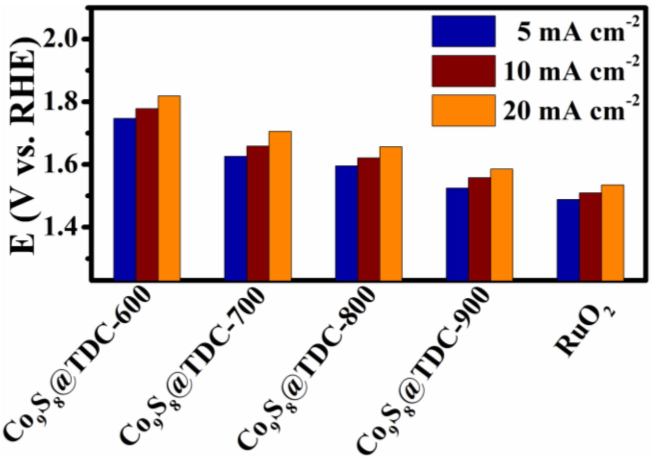

Fig. S6 a) Potentials required over Co_9S_8@TDC-600, 700, 800, 900 and RuO_2 materials to produce different current densities (5, 10, 20 mA cm^{-2}).

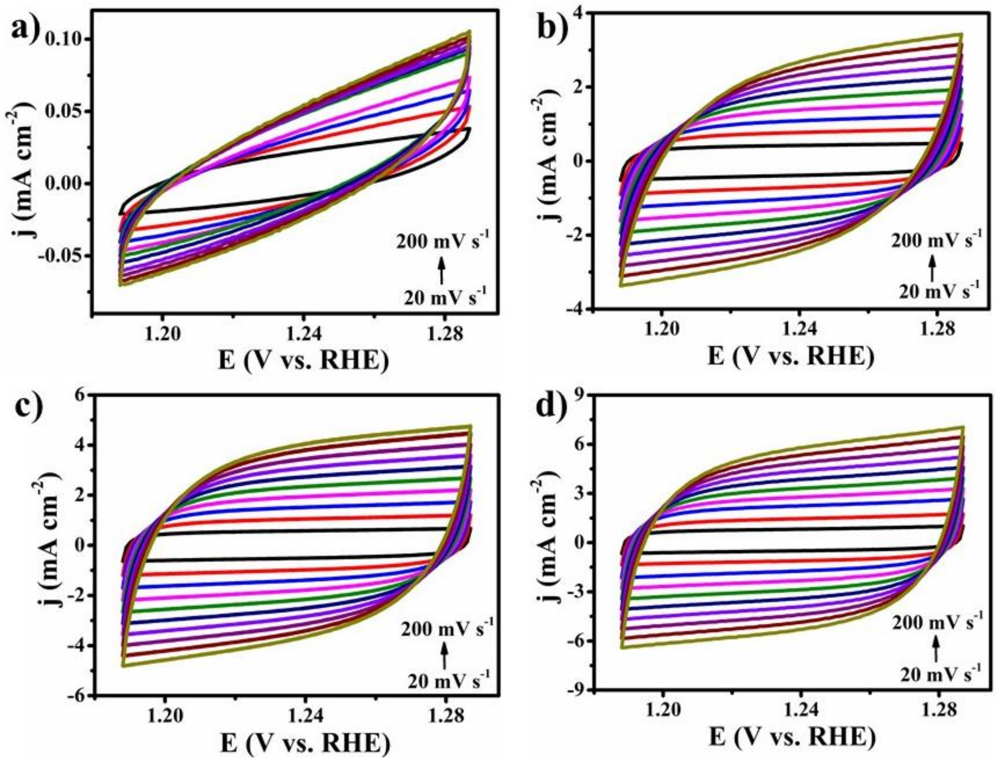

Fig. S7 CVs measured over Co_9S_8@TDC modified electrodes in the double layer capacitance charging region at scan rates of 20, 40, 60, 80, 100, 120, 140, 160, 180, and 200 mV s^{-1} in 1.0 M aqueous KOH electrolyte. The materials include: a) Co_9S_8@TDC-600; b) Co_9S_8@TDC-700; c) Co_9S_8@TDC-800 and d) Co_9S_8@TDC-900.

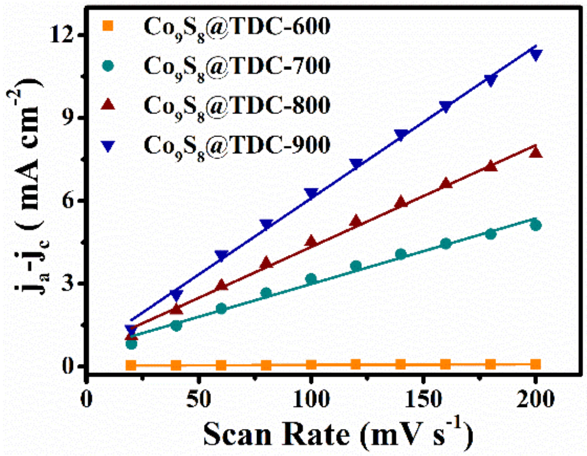

Fig. S8 Current densities (taken at a potential of 1.23 V) as a function of scan rate derived from Fig. S7, respectively.

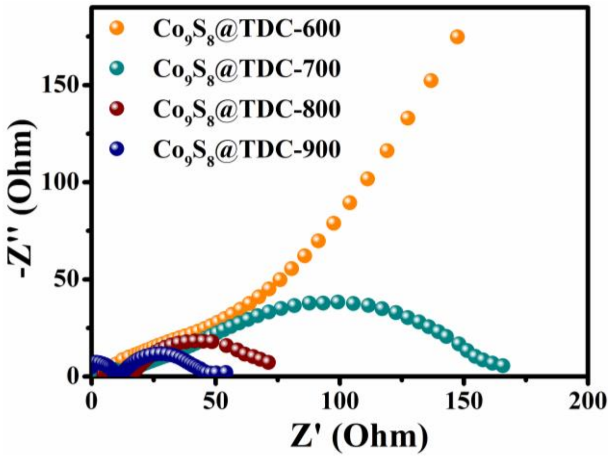

Fig. S9 EIS plots for electrodes modified with different electrocatalysts in 1.0 M KOH solution at the overpotential of 350 mV in a frequency range from 50000 Hz to 0.01 Hz.

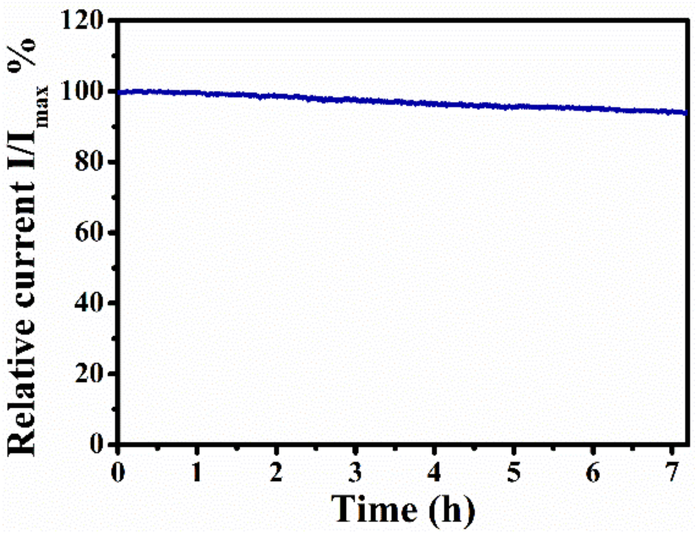

Fig. S10 Chronoamperometry curve of Co_9S_8@TDC-900 at overpotential of 350 mV.

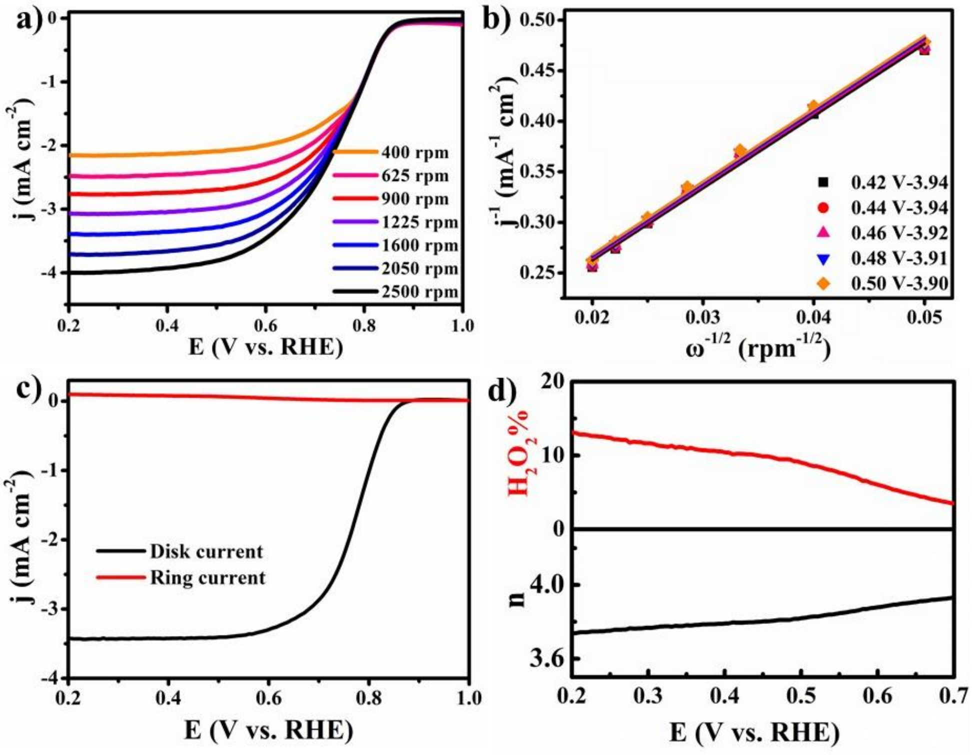

Fig. S11 a) ORR polarization curves at different rotating speeds; b) the corresponding K–L plots and electron transfer numbers (n) at different potentials of the Co_9S_8@TDC-700; c) RRDE curve for Co_9S_8@TDC-700 at 1600 rpm; d) Peroxide yield and electron transfer numbers at various potentials.

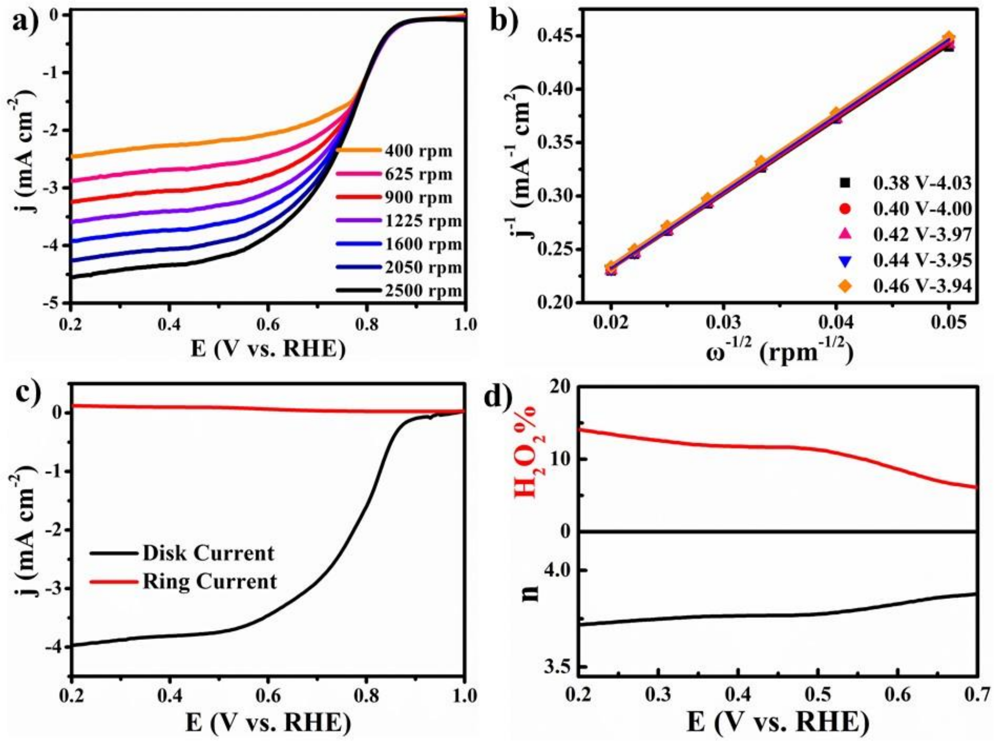

Fig. S12 a) ORR polarization curves at different rotating speeds; b) the corresponding K−L plots and electron transfer numbers (n) at different potentials of the Co_9S_8@TDC-800; c) RRDE curve for Co_9S_8@TDC-800 at 1600 rpm; d) Peroxide yield and electron transfer numbers at various potentials.

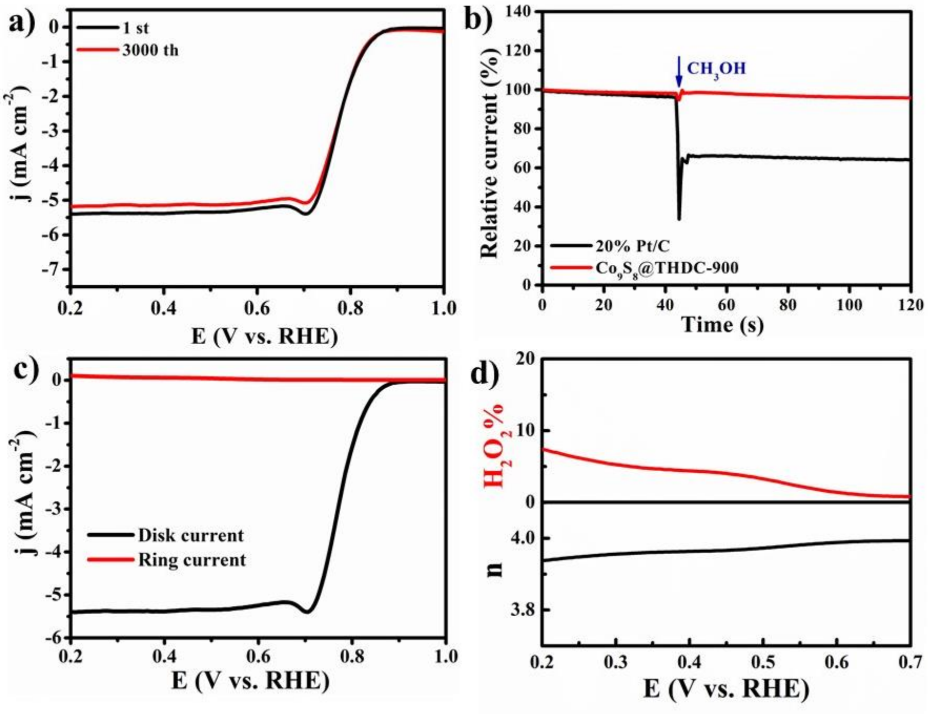

Fig. S13 a) ORR stability tests of the Co_9S_8@TDC-900, b) Methanol tolerance test for Co_9S_8@TDC-900 and Pt/C at 0.71 V in O_2-saturated and 0.1 M KOH solution at 1600 rpm; c) RRDE curve for Co_9S_8@TDC-900 at 1600 rpm; D) Peroxide yield and electron transfer numbers at various potentials.

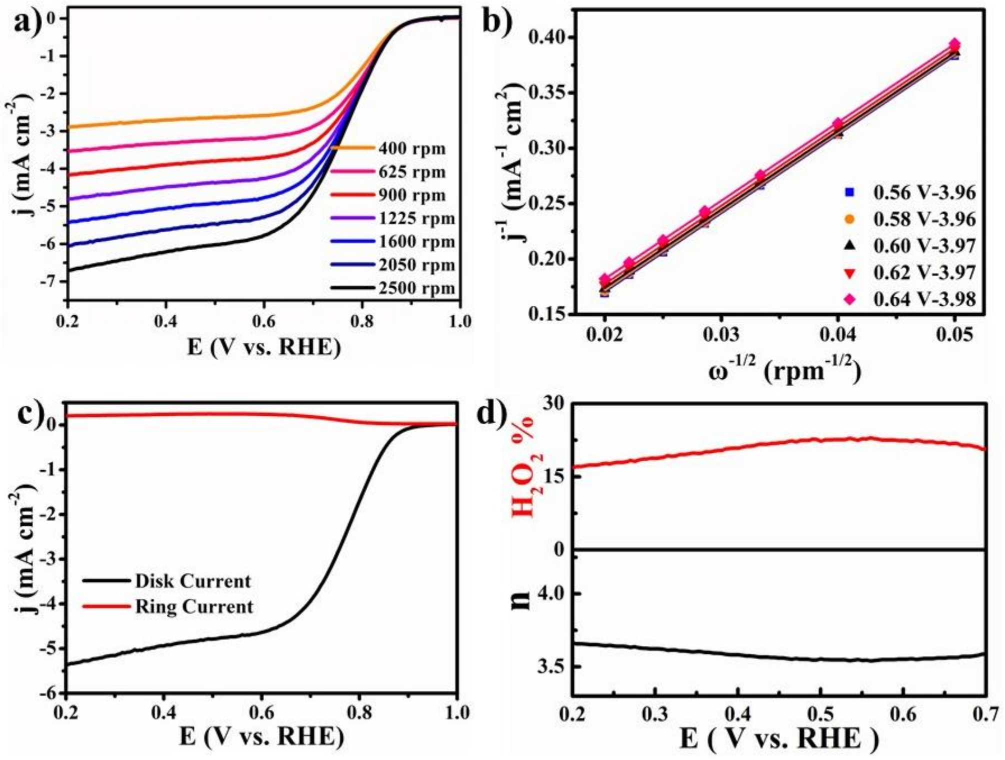

Fig. S14 a) ORR polarization curves at different rotating speeds; b) the corresponding K–L plots and electron transfer numbers (n) at different potentials of the Pt/C; c) RRDE curve for Pt/C at 1600 rpm; d) Peroxide yield and electron transfer numbers at various potentials.

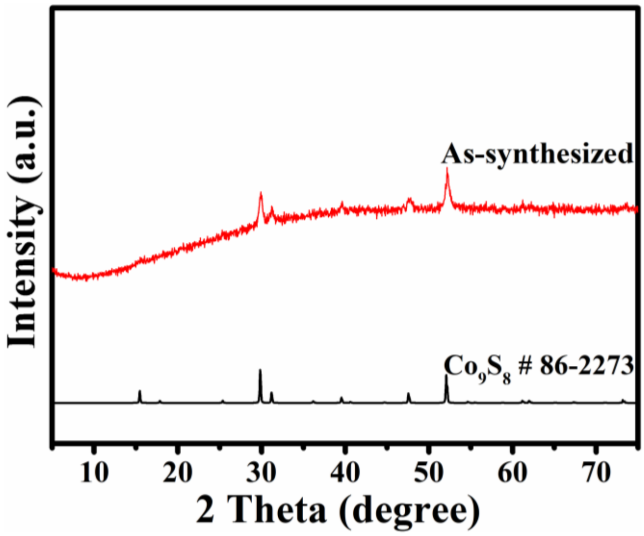

Fig. S15 PXRD pattern of the synthesized P-Co_9S_8.

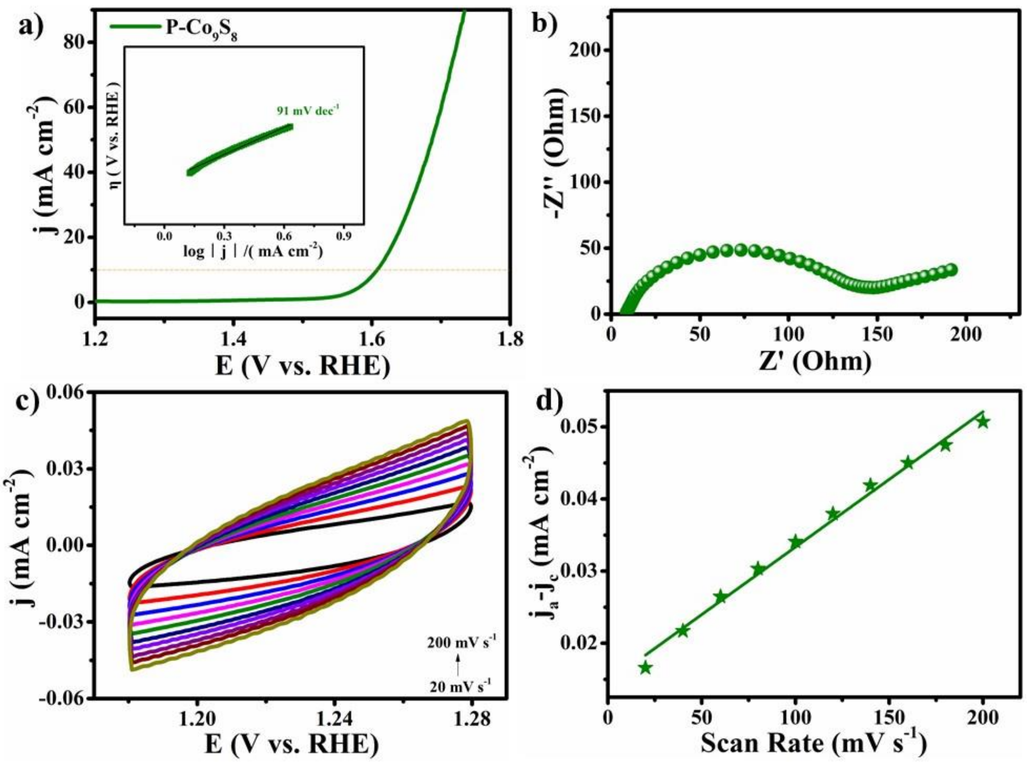

Fig. S16 OER performance of P-Co_9S_8 NPs. a) LSV curves in 1.0 M KOH. Inset: the corresponding Tafel curves. b) EIS plots for electrodes modified with P-Co_9S_8 in 1.0 M KOH solution at the overpotential of 350 mV in a frequency range from 1000 Hz to 0.01 Hz. c) CVs measured in the double layer capacitance charging region at scan rates of 20-200 mV s^{-1} in 1.0 M aqueous KOH electrolyte. d) Current densities (taken at a potential of 1.23 V) as a function of scan rate derived from c).

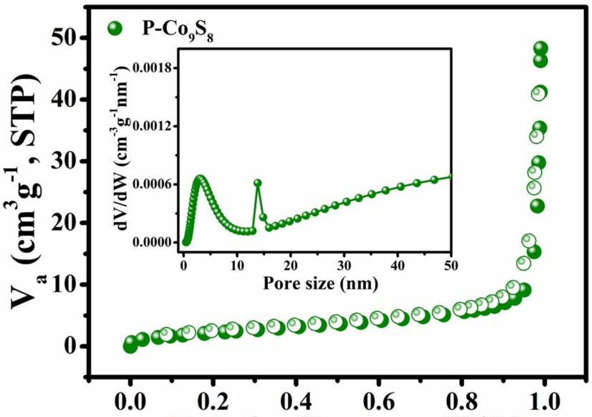

Fig. S17 The N_2 sorption isotherms at 77 K and Pore size distributions calculated by using NLDFT method of P-Co_9S_8.

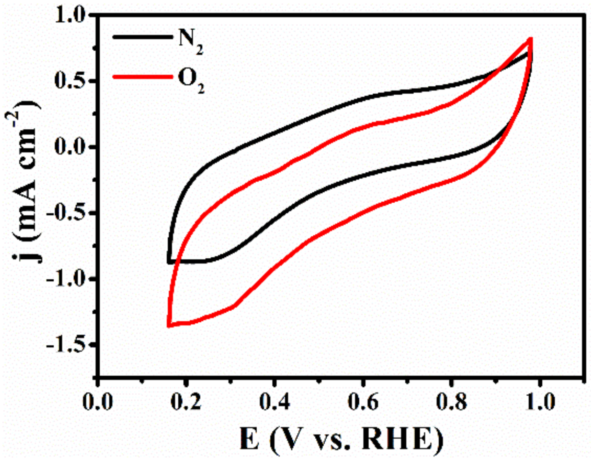

Fig. S18 CV curves of P-Co_9S_8 in O_2- and N_2-saturated 0.1 M KOH electrolyte at a scan rate of 50 mV s^{-1}.

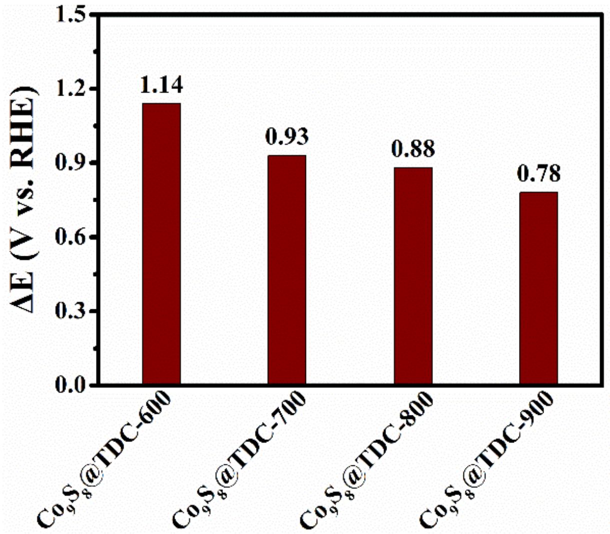

Fig. S19 The potential gap (ΔE) between $E_{j=10}$ of OER and $E_{half\text{-}wave}$ of ORR for Co_9S_8@TDC.

Table S4 Comparison of the electrocatalytic activity with non-noble OER and ORR catalysts.

Catalyst	**$E_{j=10}$**	**$E_{half\text{-}wave}$**	**$\Delta E = E_{j=10} - E_{half\text{-}wave}$**	**References**
NiO/CoN PINWs	1.53 V	0.68 V	0.85 V	[S2]
N-Co_9S_8/G	1.78 V	0.76 V	1.02 V	[7]
DG	1.57 V	0.76V	0.82 V	[S3]
$ZnCo_2O_4$	1.57 V	0.68 V	0.89 V	[S4]
CoMnO@CNT/CNF	1.60 V	0.82 V	0.78 V	[S5]
CoO/hi-Mn_3O_4	1.61 V	0.82 V	0.79 V	[S6]
Co_3Fe_7/NGNRs	1.58 V	0.78 V	0.80 V	[S7]
Co_9S_8@TDC-900	1.56 V	0.78 V	0.78V	**This work**

Table S5 Comparison of Zn-air battery performance of Co_9S_8@TDC with other state-of-the-art electrode materials.

Catalysts	**Open-circuit potential (V)**	**Peak power density (mW cm^{-2})**	**Voltage (V) at 5 mA cm^{-2}**	**Ref**
N, P co-doped mesoporous carbon foam	1.48	55	1.26	[S8]
MOF(Co)/C(3:1)	1.43	91	~1.10	[S9]
Co-PDA-C	/	/	~1.00 (2 mA cm^{-2})	[S10]
NPBC	1.47	90.7	1.15	[S11]
Co-N, B-CSs	1.43	100.0	1.35	[S12]
FeS_2/NiS_2	1.25	26.0	~1.00	[S13]
NiO/CoN PINWs	1.46	79.6	1.28 (10 mA cm^{-2})	[47]
NC-Co_3O_4-90	1.44	82.0	0.90 (10 mA cm^{-2})	[S14]
Fe@C-NG/NCNTs	1.33	101.3	~1.00 (10 mA cm^{-2})	[S15]
Co@Co_3O_4@NC-900	1.22	64.0	~0.80	[S16]
Co_9S_8@TDC-900	**1.50**	**101.5**	**1.10**	**This work**

References for Supporting Information (SI) Section

[S1] S. O. Jeon, T. Earmme and S. A. Jenekhe, *J. Mater. Chem. C*, 2014, **2**, 10129–10137.

[S2] J. Yin, Y. X. Li, F. Lv, Q. H. Fan, Y. Q. Zhao, Q. L. Zhang, W. Wang, F. Y. Cheng, P. X. Xi, and S. J. Guo, *ACS Nano*., 2017, **11**, 2275–2283.

[S3] Y. Jia, L. Z. Zhang, A. J. Du, G. P. Gao, J. Chen, X. C. Yan, C. L. Brown and X. D. Yao, *Adv. Mater.*, 2016, **28**, 9532.

[S4] J. Bao, Z. L. Wang, W. J. Liu, L. Xu, F. C. Lei, J. F. Xie, Y. Zhao, Y. P. Huang, M. L. Guan and H. M. Li, *J. Alloys*. *Compd*., 2018, **764**, 565–573.

[S5] Zhu, L. Gu, D. N. Yu, Y. J. Sun, M. Wan, M. Zhang, L. Wang, L. N. Wang, W. W. Wu, J. M. Yao, M. L. Du and S. J. Guo, *Energy Environ. Sci*., 2017, **10**, 321–330.

[S6] C. X. Guo, Y. Zheng, J. R. Ran, F. X. Xie, M. Jaroniec and S. Z. Qiao, *Angew. Chem. Int. Ed*., 2017, **56**, 8539–8543.

[S7] H. Zhang, J. Xu, Y. Jin, Y. Tong, Q. Lu, and F. Gao, *Chem. Eur. J*., 2018, **24**, 14522–14530.

[S8] J. Zhang, Z. Zhao, Z. Xia, and L. Dai, *Nat. Nanotechnol*, 2015, **10**, 444.

[S9] X. Yi, X. He, F. Yin, B. Chen, G. Li, and H. Yin, *Electrochimica Acta*, 2019, 295, 966–977.

[S10] B. Li, Y. Chen, X. Ge, J. Chai, X. Zhang, T. S. Andy Hor, G. Du, Z. Liu, H. Zhang and Y. Zong, *Nanoscale*, 2016, **8**, 5067–5075.

[S11] Q. Wang, Y. Li, K. Wang, J. Zhou, L. Zhu, L. Gu, J. Hu and X. Cao, *Electrochimica Acta*, 2017, **257**, 250–258.

[S12] Y. Guo, P. Yuan, J. Zhang, Y. Hu, I. S. Amiinu, X. Wang, J. Zhou, H. Xia, Z. Song, Q. Xu and S. Mu, *ACS Nano*., 2018, **12**, 1894−1901.

[S13] J. Jin, J. Yin, H. Liu and P. Xi, *Chin. J. Catal*., 2019, **40**, 43-51.

[S14] C. Guan, A. Sumboja, H. Wu, W. Ren, X. Liu, H. Zhang, Z. Liu, C. Cheng, S. J. Pennycook and J. Wang, *Adv. Mater*., 2017, **29**, 1704117.

[S15] Q. Wang, Y. Lei, Z. Chen, N. Wu, Y. Wang, B. Wang and Y. Wang, *J. Mater. Chem. A*, 2018, **6**, 516–526.

[S16] Z. Guo, F. Wang, Y. Xia, J. Li, A, G. Tamirat, Y. Liu, L. Wang, Y. Wang and Y. Xia, *J. Mater. Chem. A*, 2018, **6**, 1443–1453.